Author: Uitert, Edo van
Title: Weak gravitational lensing in the red-sequence cluster survey 2
Date: 2012-05-29

4

Stellar mass versus velocity dispersion as tracer of the lensing signal around galaxies

We present the results of a weak gravitational lensing analysis to determine whether the stellar mass or the velocity dispersion is more closely related to the amplitude of the lensing signal around galaxies - and hence to the projected distribution of dark matter. The lensing signal on small scales corresponds most closely to the lensing velocity dispersion in the case of a singular isothermal profile, but is on larger scales also sensitive to the clustering of the haloes. We select over 4000 lens galaxies at a redshift $z < 0.2$ with de Vaucouleur surface brightness profiles that reside in the ~300 square degree overlap between the Red Sequence Cluster Survey 2 (RCS2) and the data release 7 (DR7) of the Sloan Digital Sky Survey (SDSS). We consider both the spectroscopic velocity dispersion and the model velocity dispersion (a combination of the stellar mass, the size and the Sérsic index of a galaxy). The latter is thought to be a more reliable velocity dispersion estimator because it is calculated using quantities that are more robustly determined in the SDSS than the spectroscopic velocity dispersion. Comparing the model and spectroscopic velocity dispersion we find that they correlate well for de Vaucouleur-type galaxies. We find that the stellar mass and the spectroscopic velocity dispersion trace the amplitude of the lensing signal on small scales equally well. The model velocity dispersion, however, does significantly worse. A possible explanation is that the halo properties that determine the small-scale lensing signal - mainly the total mass - also depend on the structural parameters of galaxies, such as the effective radius and Sérsic index. We need, however, a larger lens sample to explore which combination of galaxy properties fully determine the distribution of dark matter around galaxies, which will provide valuable insights into galaxy formation processes.

E. van Uitert, H. Hoekstra, M. Franx, D.G. Gilbank, M.D. Gladders, H.K.C. Yee, to be submitted;

4.1 Introduction

Galaxies form and evolve in the gravitational potentials of large dark matter haloes. The physical processes that drive galaxy formation cause correlations between the properties of the galaxies and their dark matter haloes. Hence to gain insight into these processes, various properties of galaxies (e.g. colour, metallicity, stellar mass, luminosity, velocity dispersion) can be observed and compared (e.g. Smith et al. 2009; Graves et al. 2009). This has lead to the discovery of a large number of empirical scaling laws, such as the Faber-Jackson relation (Faber & Jackson 1976). These scaling laws help us to disentangle the processes that govern galaxy formation, and serve as important constraints for the theoretical and numerical efforts in this field. Although much progress has been made over the last few decades, many details are still unclear and warrant further investigation.

One key parameter in galaxy formation is thought to be the total mass of a galaxy. Galaxies that have more massive dark matter haloes than others attract more baryons as well, consequently form more stars which results in larger stellar masses. The relation between the stellar mass and the total mass of galaxies has been the subject of various studies based on observations (e.g. Mandelbaum et al. 2006; van Uitert et al. 2011; Leauthaud et al. 2012; More et al. 2011; Wake et al. 2011) and simulations (e.g. Guo et al. 2010; Moster et al. 2010), and the two components are indeed found to be correlated. Another property of galaxies that is related to the total mass is the velocity dispersion, the luminosity weighted dispersion of the motions of stars along the line-of-sight within a spectroscopic aperture. The velocity dispersion provides a dynamical estimate of the central mass, and correlates with the stellar mass (Taylor et al. 2010) and the total mass of galaxies (van Uitert et al. 2011).

A fundamental question that is of interest in this context is which property of galaxies is most tightly correlated to the total mass. This is interesting, because it shows which property in the centre of dark matter haloes is most intimately linked to the large-scale potential, and is therefore least sensitive to galaxy formation processes such as galaxy mergers and supernova activity that introduce scatter in these relations. The properties of galaxies we compare in this work are the stellar mass and the velocity dispersion. Note that there are various other observables that trace the total mass, and could have been used instead, but most of them are either expected to exhibit a large amount of scatter (e.g. metallicity), or they are directly related to the stellar mass (e.g. luminosity).

The total mass of galaxies is not directly observable, and can only be determined by indirect means. An excellent tool to do this is via weak gravitational lensing. In weak lensing the distortion of the images of faint background galaxies (sources) due to the gravitational potentials of intervening structures (lenses) is measured. From this distortion, the differential surface mass density of the lenses can be deduced, which can be modelled to obtain the total mass. A major advantage of gravitational lensing over other methods that aim to determine the total mass is that it does not rely on optical tracers. Dark matter haloes of galaxies generally extend over hundreds of kpcs, but at large distances no optical tracers can be used. This complicates studies that rely on optical tracers to determine the total mass. This does not affect weak lensing, as the distortion can be measured for any galaxy, out to very large radii (several Mpcs).

The major disadvantage of weak lensing is that the lensing signal of individual galaxies is too weak to detect as the induced distortions are typically 10-100 times smaller than the intrinsic ellipticities of galaxies. Therefore, the signal has to be averaged over hundreds or thousands of lenses to yield a useful signal. However, the average total mass for a certain selection of galaxies is still a very useful measurement, which can be compared to simulations.

It is important to note that the lensing signal on small and large scales measures different properties of the dark matter haloes. On small scales, within the virial radius, the lensing signal traces the dark matter distribution of the halo that hosts the galaxy and is therefore directly related to the halo mass. On projected separations larger than a few times the virial radius, however, the lensing signal is mainly determined by neighbouring structures, and therefore depends on the clustering properties of the lens sample under investigation. In this work, we ignore the lensing signal at large scales and focus at the signal at small scales, which mainly depends on the halo mass of galaxies.

The outline of this work is as follows. In Section 4.2, we discuss the various steps of the lensing analysis: we start with a description of the lens selection, then provide a brief outline of the creation of the shape measurement catalogues, and finally discuss the lensing analysis. The measurements are shown in Section 4.3, and we conclude in Section 4.4. Throughout the paper we assume a WMAP7 cosmology (Komatsu et al. 2011) with $\sigma_8 = 0.8$, $\Omega_\Lambda = 0.73$, $\Omega_M = 0.27$, $\Omega_b = 0.046$ and $h = 0.7$ the dimensionless Hubble parameter. All distances quoted are in physical (rather than comoving) units unless explicitly stated otherwise.

4.2 Lensing analysis

In this study we use the ~300 square degrees of overlapping area between the Sloan Digital Sky Survey (SDSS; York et al. 2000) and the Red Sequence Cluster Survey 2 (RCS2; Gilbank et al. 2011). We use the SDSS to obtain the properties of the lenses (e.g. stellar mass, velocity dispersion), information that is not available in the RCS2. The lensing analysis is performed on the RCS2, because it is ~2 magnitudes deeper than the SDSS in r'. The increase in depth combined with a median seeing of $0.7''$, which is a factor of two smaller than the seeing in the SDSS, results in a source galaxy number density that is about five times higher, and a source redshift distribution that peaks at $z{\sim}0.7$. Therefore, the RCS2 enables a high-quality detection of the lensing signal, even for a moderate number of lens galaxies.

4.2.1 Lenses

The SDSS has imaged roughly a quarter of the entire sky, and has measured the spectra for about one million galaxies (Eisenstein et al. 2001; Strauss et al. 2002). The combination of spectroscopic coverage and photometry in five optical bands (u, g, r, i, z) in the SDSS provides a wealth of galaxy information that is not available from the RCS2. To use this information, but also benefit from the improved lensing quality of the RCS2, we use the 300 square degrees overlap between the surveys for our analysis. We match the RCS2 catalogues to the DR7 (Abazajian et al. 2009) spectroscopic catalogue, to the MPA-JHU

DR7[1] stellar mass catalogue and to the NYU Value Added Galaxy Catalogue (NYU-VAGC)[2] (Blanton et al. 2005; Adelman-McCarthy et al. 2008; Padmanabhan et al. 2008) which yields the spectroscopic redshifts, velocity dispersions, and the stellar masses of 1.7×10^4 galaxies. From these galaxies we select our lenses using criteria that are detailed below.

The spectroscopic fibre within which the velocity dispersion is measured has a fixed size. The physical region where the velocity dispersion is averaged is therefore different for a sample of galaxies with different sizes and redshifts. To account for this, we follow Bezanson et al. (2011) and scale the observed spectroscopic velocity dispersion to a fixed size of $R_e/8$ using $\sigma_{\rm spec} = \sigma_{\rm spec}^{\rm ap}(8.0 r_{\rm ap}/R_e)^{0.066}$, with $r_{\rm ap}$=1.5″ the radius of the SDSS spectroscopic fiber, R_e the effective radius in the r-band, and $\sigma_{\rm spec}^{\rm ap}$ the observed velocity dispersion. This correction is based on the best-fit relation determined using 40 galaxies in the SAURON sample (Cappellari et al. 2006). However, the spectroscopic velocity dispersions provided in the DR7 spectroscopic catalogues are generally noisy for exponential galaxies. To obtain more reliable velocity dispersion estimates for these galaxies, we also predict the velocity dispersion based on quantities that are more robustly determined following Bezanson et al. (2011):

$$\sigma_{\rm mod} = \sqrt{\frac{GM_*}{0.557 K_V(n) R_e}} \tag{4.1}$$

with M_* the stellar mass, n the Sérsic index and $K_V(n)$ a term that includes the effects of structure on stellar dynamics, and can be approximated by (Bertin et al. 2002)

$$K_V(n) \cong \frac{73.32}{10.465 + (n - 0.94)^2} + 0.954. \tag{4.2}$$

The equation for $\sigma_{\rm mod}$ is based on the results of Taylor et al. (2010), who demonstrated that the structure-corrected dynamical mass is linearly related to the stellar mass for a selection of low-redshift galaxies in the SDSS.

The stellar mass estimates in the MPA-JHU DR7 catalogues are based on the model magnitudes. The Sérsic index and the effective radius in Equation (4.1), however, correspond to a different flux, i.e. the Sérsic model flux, which is the total flux of the best fit Sérsic model. This flux is also provided in the NYU-VAGC catalogue, and differs slightly from the model flux. To calculate $\sigma_{\rm mod}$ consistently, we therefore scale the stellar mass with the ratio of the model flux to the Sérsic model flux.

Bezanson et al. (2011) find that the model and the observed velocity dispersion correlate very well in the range 60 km s^{-1} $< \sigma <$ 300 km s^{-1}, for galaxies in the redshift range $0.05 < z < 0.07$, and for a few galaxies with redshifts $1 < z < 2.5$. The SDSS spectroscopic sample extends to $z \sim 0.5$, and therefore contains many more massive galaxies. To determine whether the velocity dispersions correlate well in this range too, we compare the dispersions for the complete SDSS spectroscopic sample in Figure 4.1. We find that the velocity dispersions agree well, though at $z > 0.2$ the range in velocity dispersion becomes too small to assess whether the velocity dispersions are still correlated.

To study whether the spectroscopic velocity dispersion and the model

[1]http://www.mpa-garching.mpg.de/SDSS/DR7/
[2]http://sdss.physics.nyu.edu/vagc/

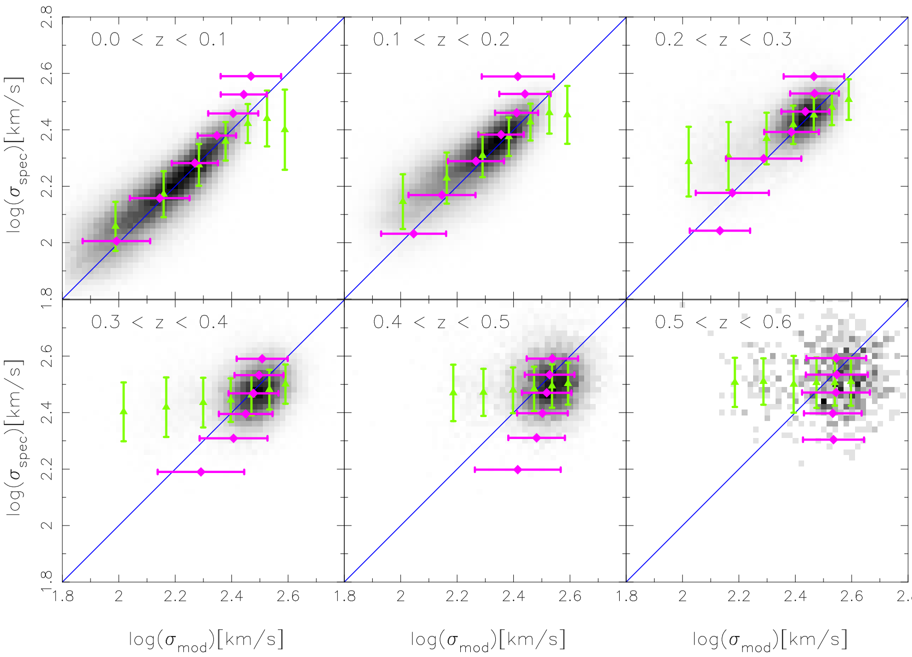

Figure 4.1: Comparison of the spectroscopic velocity dispersions to the model velocity dispersions for all galaxies with SDSS spectroscopy. The green triangles show the average spectroscopic velocity dispersion for bins of model velocity dispersion, the purple diamonds show the average model velocity dispersion for bins of spectroscopic velocity dispersion. The error bars indicate the scatter. The blue line shows the one-to-one correspondence. Only galaxies with a spectroscopic velocity dispersion error smaller than 15% have been used in the comparison. The velocity dispersions correlate well at $z < 0.2$, but at $z > 0.2$ the range in velocity dispersion becomes too small to assess whether this is still the case .

velocity dispersion agree equally well for de Vaucouleur and exponential galaxies, we split the galaxies based on their *frac_dev* parameter from the SDSS photometric catalogues. This parameter is determined by simultaneously fitting $frac\_deV$ times the best-fitting De Vaucouleur profile plus (1-$frac\_deV$) times the best-fitting exponential profile to an object's brightness profile. The *frac_dev* parameter is therefore a measure of the slope of the brightness profile of a galaxy; galaxies with *frac_dev* > 0.5 predominantly have a de Vaucouleurs profile, and *frac_dev* < 0.5 an exponential profile. We select all galaxies with redshifts $z < 0.2$, and show the comparison in Figure 4.2. We find that for the de Vaucouleur galaxies, the spectroscopic and model velocity dispersion agree very well. For the exponentials, however, we find that the spectroscopic velocity dispersion is ∼0.1 dex higher than the model velocity dispersion. This is not surprising: Taylor et al. (2010) found that the relation between the stellar mass and the structure-corrected dynamical mass has a weak dependence on the Sérsic index, i.e. the ratio of the stellar mass and the dynamical mass increases with increasing Sérsic index (see Figure 14 in Taylor et al. 2010). The offset in the relation between spectroscopic and model velocity dispersion for exponen-

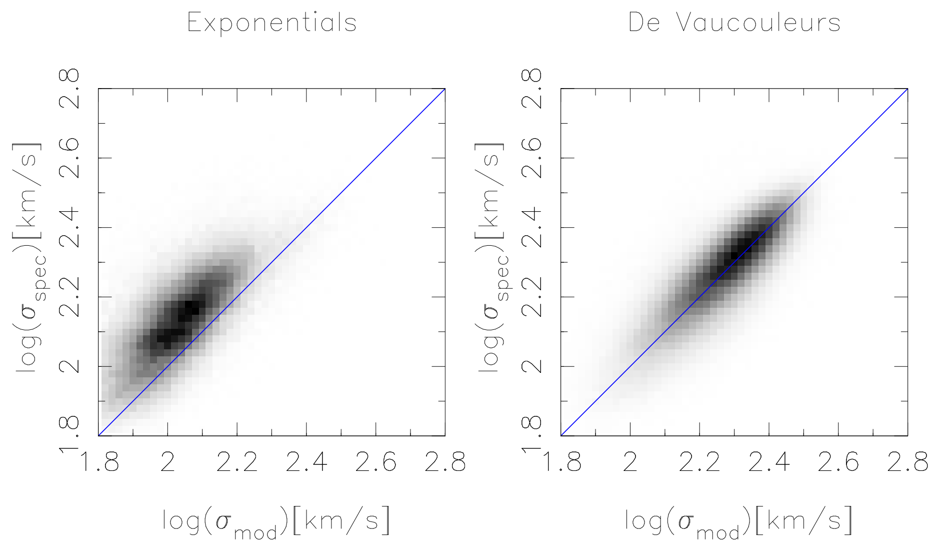

Figure 4.2: Comparison of the spectroscopic velocity dispersions to the model velocity dispersions for exponential galaxies (*left*) and de Vaucouleur galaxies (*right*) in the redshift range $0 < z < 0.2$. For de Vaucouleurs, the dispersions agree very well, but for exponential galaxies, we find that the spectroscopic velocity dispersion is roughly 0.1 dex higher than the model velocity dispersion.

tial galaxies is a direct consequence. It might be caused by the contribution of the disk velocity of spiral galaxies to the spectroscopic velocity dispersion. One could in principle apply a Sérsic index dependent correction, but we choose to use only de Vaucouleur galaxies, because there are very few exponentials in the velocity dispersion range we are interested in.

In Figure 4.3, we plot the spectroscopic and model velocity dispersion as a function of stellar mass. We only select galaxies with redshifts $z < 0.2$; at higher redshifts, the range in velocity dispersions is too small to establish whether the correlation works well. The three lens samples we use are indicated by the dashed lines. We select all de Vaucouleur galaxies with a stellar mass $10.8 < \log(M_*) < 11.5$ in units of $h_{70}^{-1}M_\odot$; all de Vaucouleur galaxies with a model velocity dispersion 180 km s$^{-1} < \sigma_{\rm mod} < 300$ km s^{-1}; and all de Vaucouleurs with a spectroscopic velocity dispersion 200 km s$^{-1} < \sigma_{\rm spec} < 300$ km s^{-1} and $\delta\sigma_{\rm spec}/\sigma_{\rm spec} < 0.15$. With these criteria we select 4735, 4218 and 4317 lenses respectively, and they form the lens samples of this study.

4.2.2 Data reduction

The RCS2 is a nearly 900 square degree imaging survey in three bands (g', r' and z') carried out with the Canada-France-Hawaii Telescope (CFHT) using the 1 square degree camera MegaCam. The photometric calibration of the RCS2 is described in detail in Gilbank et al. (2011). The magnitudes are calibrated using the colours of the stellar locus and the overlapping Two-Micron All-Sky Survey (2MASS), and are accurate to < 0.03 mag in each band compared to the SDSS. The creation of the galaxy shape catalogues is described in detail in van Uitert et al. (2011). We refer readers to that paper for more detail, and present

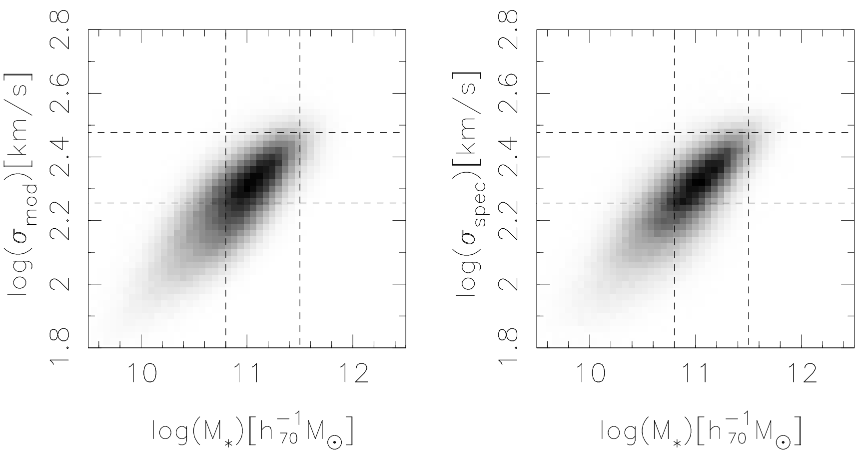

Figure 4.3: Model velocity dispersion (*left*) and spectroscopic velocity dispersion (*right*) as a function of stellar mass. The dashed lines indicate the selection cuts for the lenses.

here a short summary of the most important steps.

We retrieve the Elixir[3] processed images from the Canadian Astronomy Data Centre (CADC) archive[4]. We use the THELI pipeline (Erben et al. 2005, 2009) to subtract the image backgrounds, create weight maps that we use in the object detection phase, and to identify satellite and asteroid trails. To detect the objects in the images, we use `SExtractor` (Bertin & Arnouts 1996). The stars that are used to model the PSF variation across the image are selected using size-magnitude diagrams. All objects larger than 1.2 times the local size of the PSF are identified as galaxies. We measure the shapes of the galaxies with the KSB method (Kaiser et al. 1995; Luppino & Kaiser 1997; Hoekstra et al. 1998), using the implementation described by Hoekstra et al. (1998, 2000). This implementation has been tested on simulated images as part of the Shear Testing Programme (STEP) 1 and 2 (the 'HH' method in Heymans et al. 2006 and Massey et al. 2007 respectively), and these tests have shown that it reliably measures the unconvolved shapes of galaxies for a variety of PSFs. Finally, we correct the source ellipticities for camera shear, a false shear signal which originates from slight non-linearities in the camera optics. The resulting shape catalogue of the RCS2 contains the ellipticities of 2.2×10^7 galaxies, from which we select the subset of approximately 1×10^7 galaxies that coincides with the SDSS.

4.2.3 Lensing measurement

In weak lensing, the ellipticities of the source galaxies are used to measure the azimuthally averaged tangential shear around the lenses as a function of projected separation:

$$\langle\gamma_t\rangle(r) = \frac{\Delta\Sigma(r)}{\Sigma_{\rm crit}}, \tag{4.3}$$

[3]http://www.cfht.hawaii.edu/Instruments/Elixir/
[4]http://www1.cadc-ccda.hia-iha.nrc-cnrc.gc.ca/cadc/

where $\Delta\Sigma(r) = \bar{\Sigma}(< r) - \bar{\Sigma}(r)$ is the difference between the mean projected surface density enclosed by r and the mean projected surface density at a radius r, and $\Sigma_{\rm crit}$ is the critical surface density:

$$\Sigma_{\rm crit} = \frac{c^2}{4\pi G}\frac{D_s}{D_l D_{ls}}, \tag{4.4}$$

with D_l, D_s and D_{ls} the angular diameter distance to the lens, the source, and between the lens and the source, respectively. Since we lack redshifts for the background galaxies, we select galaxies with $22 < m_{r'} < 24$ that have a reliable shape estimate (ellipticities smaller than one, no SExtractor flag raised) as sources. We obtain the approximate source redshift distribution by applying identical magnitude cuts to the photometric redshift catalogues of the Canada-France-Hawaii-Telescope Legacy Survey (CFHTLS) "Deep Survey" fields (Ilbert et al. 2006).

To correct the signal for systematic contributions, we subtract the random shear signal from the measured source ellipticities. Details on the calculation of this correction can be found in van Uitert et al. (2011). Note that this correction mostly affects large scales (>20 arcmin), as on small scales the lensing signal is generally averaged over many lens-source orientations causing the systematic contributions to average out. As the lenses and sources barely overlap in redshift, we do not have to correct the lensing signal for the contamination of physically associated galaxies in the source sample. The source galaxy overdensity near the lenses is found to be a few percent at most, confirming that this correction is unimportant.

Although neither the dark matter nor the baryonic component are well described by a singular isothermal sphere (SIS), the sum of the two components is remarkably close (e.g. Treu & Koopmans 2004; Koopmans et al. 2009). The SIS signal is given by

$$\gamma_{t,{\rm SIS}}(r) = \frac{r_E}{2r} = \frac{4\pi\sigma^2_{\rm lens}}{c^2}\frac{D_l D_{ls}}{D_s}\frac{1}{2r}, \tag{4.5}$$

where r_E is the Einstein radius and $\sigma_{\rm lens}$ the lensing velocity dispersion. Based on the range of stellar masses and velocity dispersions of our lenses, we expect the majority of lenses to be central galaxies (see, e.g. van Uitert et al. 2011 or Mandelbaum et al. 2006 for estimates of the satellite fraction for galaxies in these ranges). Therefore, the lensing signal of our galaxies should be reasonably well described by an SIS profile over a relatively large range of projected separations.

To determine whether the stellar mass or the velocity dispersion is a better tracer of the amplitude of the lensing signal, we would ideally select lenses in a very narrow range in stellar mass, split those in a high and low velocity dispersion bin, and compare their lensing signals. A difference between the lensing signal of the low and high velocity dispersion would indicate a residual dependence on velocity dispersion. Similarly, we would like to select lenses in a very narrow range of velocity dispersion, split them in stellar mass and compare their signals. Comparing the lensing signals of these four bins would allow us to determine whether the stellar mass or the velocity dispersion is more closely related to the lensing signal on small scales - and hence to the projected distribution of dark matter. Unfortunately, we do not have a sufficient number of lenses for this approach.

Instead, we have to select lenses that cover a larger range in stellar mass (and velocity dispersion). We cannot simply split the lenses in velocity dispersion and compare their lensing signals, because the stellar mass and velocity dispersion are correlated, and the high velocity dispersion bin also has a larger mean stellar mass. To account for this, we determine how the lensing signal scales with stellar mass, and subtract this trend from the high and low velocity dispersion bins. We also determine how the lensing signal scales with velocity dispersion, and remove this trend from the high and low stellar mass bin. If the lensing signal of galaxies strongly depends on the velocity dispersion, but only weakly on stellar mass, we expect a clear positive difference between the high and low velocity dispersion bins after we removed the trend with stellar mass. At the same time, we should see only a very small difference between the high and low stellar mass bin after removing the trend with velocity dispersion. Hence by studying the differences in the residual lensing signals, we can tell which observable is more closely related to the lensing signal of galaxies.

4.3 Results

To study whether the lensing signal mainly depends on stellar mass or velocity dispersion, we first have to determine how the lensing signal scales with these observables. We discuss how this is done for the model velocity dispersion; for the spectroscopic velocity and the stellar mass, we follow a similar approach. The general procedure is summarized below.

- We sort the lenses in model velocity dispersion, and divide them in five quintiles;
- We measure the lensing signal of each quintile, to which we fit an SIS profile on scales between 50 h_{70}^{-1}kpc and 1 h_{70}^{-1}Mpc. This is roughly the range where the galaxy dark matter halo dominates the lensing signal. This results in five best-fit lensing velocity dispersions, $\sigma_{\rm lens}$;
- We use the five values of $\sigma_{\rm lens}$ to fit the linear relation $\sigma_{\rm lens} = a_{\rm mod} \times (\sigma_{\rm mod}/200\,{\rm km\,s^{-1}}) + b_{\rm mod}$. We show the measurements and the fit in Figure 4.4, and give the best-fit parameters in Table 4.1;
- We determine the median stellar mass of these lenses, and divide them into a low and high stellar mass sample. We measure the lensing signal of both samples, and show them in the top-left panel of Figure 4.5;
- For each lens in the low and high stellar mass sample, we use the model velocity dispersion to calculate $\sigma_{\rm lens}$ using the linear relation, and subtract their SIS profiles from the lensing signal. The residuals are shown in the middle-left panel of the same figure;
- Finally, we determine the difference between the residual lensing signal of the high and low stellar mass bin, $\delta(\Delta\Sigma - \Delta\Sigma_{\rm trend})$, which is shown in the bottom-left panel.

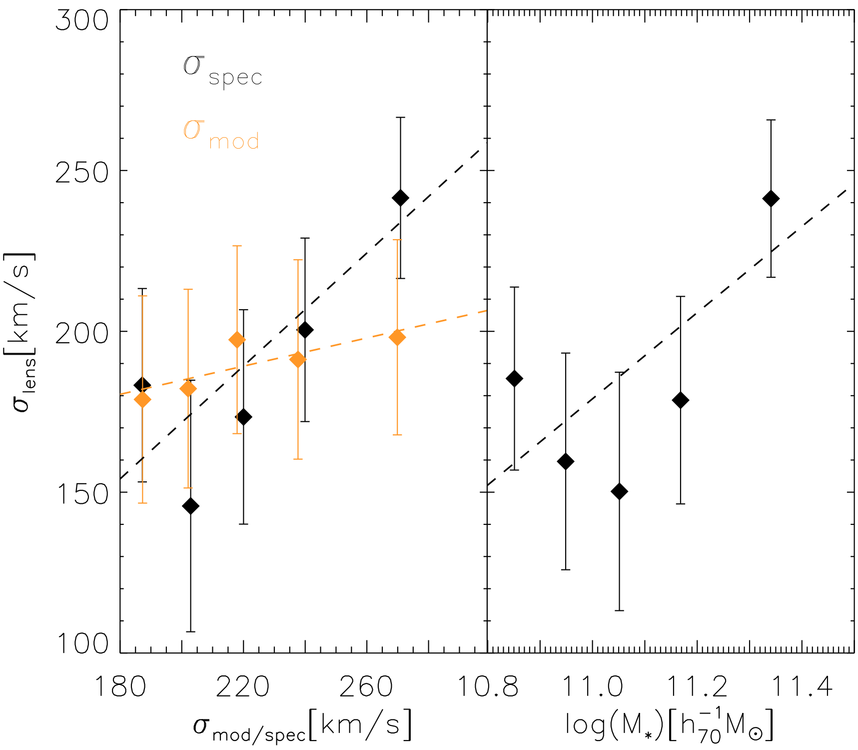

Figure 4.4: Best-fit lensing velocity dispersion as a function of spectroscopic velocity dispersion (*left panel, black*), model velocity dispersion (*left panel, orange*) and stellar mass (*right panel*). Dashed lines indicate the best-fit linear relation between the observable and $\sigma_{\rm lens}$. The linear relations are used to remove the dependence of the lensing signal on these observables.

When we subtract two SIS profiles with different amplitudes from each other, the result is also an SIS profile. Therefore, to quantify the residuals, we fit an SIS to $\delta(\Delta\Sigma - \Delta\Sigma_{\rm trend})$ on the same scales, and determine the residual Einstein radius, $r_E^{\rm res}$. These values can be found in Table 4.2.

Similarly, we determine the dependence of the lensing signal on spectroscopic velocity dispersion and stellar mass. For the spectroscopic velocity dispersion, we fit $\sigma_{\rm lens} = a_{\rm spec} \times (\sigma_{\rm spec}/200\,{\rm km\ s^{-1}}) + b_{\rm spec}$ and for the stellar mass, we fit $\sigma_{\rm lens} = a_{\rm stel} \times \log(M_*/10^{11}\,h_{70}^{-1} M_\odot) + b_{\rm stel}$. The best-fit parameters are shown in Table 4.1. These trends are removed from the lensing signals, and the residuals are shown in Figure 4.5 (middle panel).

From the bottom panels of the first and second columns of Figure 4.5, we observe that if we remove the dependence on model velocity dispersion, the lensing signal still depends on stellar mass. When we remove the dependence on

Table 4.1: Best-fit powerlaw parameters that describe the relation between the galaxy property and the lensing velocity dispersion in the indicated range. Details of the fitting are described in the text.

$\sigma_{\rm mod}$ [km/s]	$a_{\rm mod}$ [km/s]	$b_{\rm mod}$ [km/s]
$180 < \sigma_{\rm mod} < 300$	44 ± 96	141 ± 108
$100 < \sigma_{\rm mod} < 400$	93 ± 49	80 ± 50
$\sigma_{\rm spec}$ [km/s]	$a_{\rm spec}$ [km/s]	$b_{\rm spec}$ [km/s]
$180 < \sigma_{\rm spec} < 300$	176 ± 86	-5 ± 100
$100 < \sigma_{\rm spec} < 400$	129 ± 42	45 ± 45
$\log(M_*)$ [$h_{70}^{-1} M_\odot$]	$a_{\rm stel}$ [km/s]	$b_{\rm stel}$ [km/s]
$10.8 < \log(M_*) < 11.5$	134 ± 71	179 ± 15
$10.5 < \log(M_*) < 12.0$	118 ± 44	178 ± 12

Table 4.2: The residual Einstein radius, obtained by fitting an SIS profile to $\delta(\Delta\Sigma - \Delta\Sigma_{\rm trend})$ between 50 h_{70}^{-1}kpc and 1 h_{70}^{-1}Mpc for a mean lens redshift of $z = 0.13$. The bracketed values show the results for a different linear relation between the observable and $\sigma_{\rm lens}$, as detailed in the text.

removed trend	residual dependence	$r_E^{\rm res}$ [h_{70}^{-1}kpc]	
$\sigma_{\rm mod}$	M_*	0.88 ± 0.25	(0.78 ± 0.25)
M_*	$\sigma_{\rm mod}$	-0.18 ± 0.24	(-0.12 ± 0.24)
$\sigma_{\rm spec}$	M_*	0.30 ± 0.25	(0.42 ± 0.25)
M_*	$\sigma_{\rm spec}$	0.37 ± 0.24	(0.42 ± 0.24)

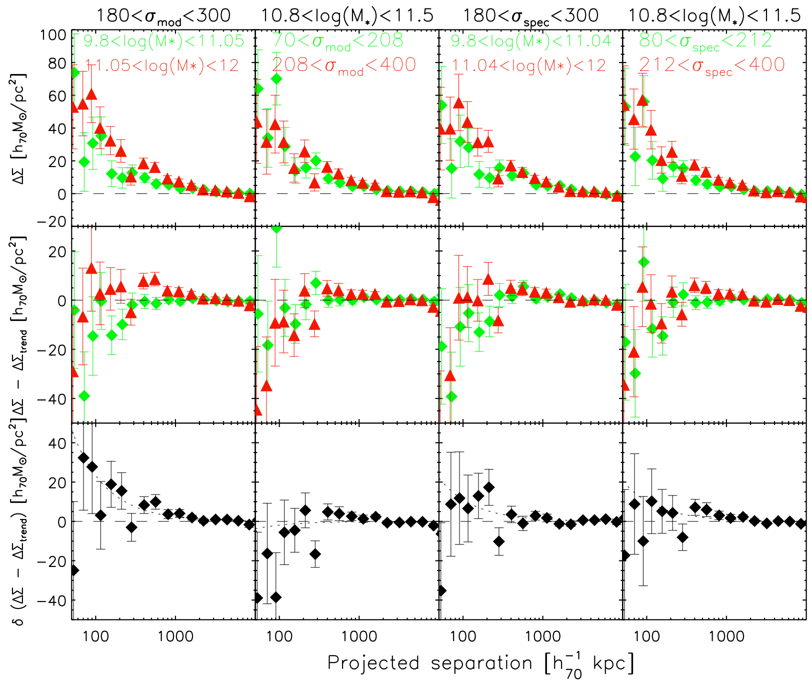

Figure 4.5: In the top row, we show the lensing signal $\Delta\Sigma$ as a function of physical distance from the lens, for the lens samples that have been split by the median value of one of the observables, as indicated in the plots. Red triangles (green diamonds) indicate the signal of the lenses with larger (smaller) stellar masses/velocity dispersions. In the middle row, we show the lensing signal of the same samples after we subtracted the trend with the observable that is indicated on top of each column. The difference between the residual trends for the two lens samples are shown in the bottom row. The dotted lines show the best-fit SIS profiles to the difference between the residuals.

stellar mass, the difference between the residuals of the model velocity samples is consistent with zero. These trends are reflected by the values for $r_E^{\rm res}$ in Table 4.2. The third and fourth columns of Figure 4.5 show that if we remove the dependence on spectroscopic velocity dispersion, the difference of the residual signal of the high and low stellar mass sample is consistent with the difference between the residual signal of the high and low spectroscopic velocity dispersion samples after we removed the dependence on stellar mass.

These results suggest that the stellar mass is a better tracer of the lensing signal of galaxies than the model velocity dispersion. Furthermore, the stellar mass and the spectroscopic velocity dispersion trace the lensing signal equally well, as the residual Einstein radii are consistent. As a consistency test, we have also looked at the residual dependence on model velocity dispersion after removing the trend with spectroscopic velocity dispersion, and vice versa. These trends confirm our previous findings: the spectroscopic velocity dispersion is more sensitive to the lensing signal of galaxies than the model velocity dispersion.

There is a weak indication that the lensing signal has a residual dependence on stellar mass after we remove the trend with spectroscopic velocity dispersion, and vice versa. This would imply that both the stellar mass and the velocity dispersion contain independent information on the projected distribution of dark matter around galaxies. Unfortunately, we do not have sufficient signal-to-noise to obtain a clear detection.

The results depend on the linear relations we have fit to remove the dependence on the observables. To study how sensitive the residual trends are on these relations, we have also fit them using all de Vaucouleur galaxies in the range 100 km s^{-1} $< \sigma_{\rm spec} <$ 400 km s^{-1}, 100 km s^{-1} $< \sigma_{\rm mod} <$ 400 km s^{-1} and $10.5\ h_{70}^{-1} M_{\odot} < \log(M_*) < 12\ h_{70}^{-1} M_{\odot}$, respectively. The best-fit parameters of these fits are shown in Table 4.1. We repeated the analysis using these values, and show the residual Einstein radii between brackets in Table 4.2. We find that this does not significantly change the results, i.e. the model velocity dispersion traces the lensing signal of galaxies worse than either the stellar mass or the spectroscopic velocity dispersion.

It is somewhat surprising that $\sigma_{\rm mod}$ is a poorer tracer of the total mass than $\sigma_{\rm spec}$, particularly because we observe in Figure 4.1 that they correlate well. To study where the samples differ, we plot the average effective radii and Sérsic indices as a function $\sigma_{\rm mod}$ and $\sigma_{\rm spec}$ in Figure 4.6. We find that at low velocity dispersions, the values of r_e and n are similar, but at high velocity dispersions, the lenses in the $\sigma_{\rm spec}$ samples have larger effective radii, whilst the lenses in the $\sigma_{\rm mod}$ have larger Sérsic indices. Hence the difference between the performance of $\sigma_{\rm mod}$ and $\sigma_{\rm spec}$ could be due to an additional dependence of the lensing signal on the structural parameters of the lenses.

To test whether the lensing signal depends on the size of galaxies, we select the lenses from the model velocity dispersion sample, and remove the lensing signal dependence on $\sigma_{\rm mod}$. Then we determine the median effective radius, split the lenses into a low and high effective radius sample and measure their residual lensing signal. As before, we measure the difference between the residual lensing signals of the high and low effective radius sample, to which we fit an SIS profile. We find $r_E^{\rm res} = 0.53 \pm 0.25\ h_{70}^{-1}$ kpc, which suggests that the lensing signal depends on the size of a galaxy. However, in Figure 4.7 we find that the effective radius is correlated with stellar mass, so part of this residual may be caused by the dependence on stellar mass. Therefore, we repeat the test using the lenses from the stellar mass sample, and remove the lensing signal dependence on stellar mass. Then we determine the median effective radius, split the lenses into a low and high effective radius sample and measure the difference between their residual lensing signals. We find $r_E^{\rm res} = 0.14 \pm 0.24\ h_{70}^{-1}$ kpc. Studying the residual dependence on Sérsic index, we find $r_E^{\rm res} = 0.04 \pm 0.25\ h_{70}^{-1}$ kpc for the model velocity dispersion sample, and $r_E^{\rm res} = 0.11 \pm 0.24\ h_{70}^{-1}$ kpc for the stellar mass sample. These results do not provide conclusive evidence that the small-scale lensing signal depends on these structural parameters.

Although the three lens samples overlap, they are not identical. Hence part of the trends we observe might actually be due to differences in the lens samples. To test this, we could define a fourth sample by selecting galaxies that pass all selection criteria, i.e. 180 km s^{-1} $< \sigma_{\rm mod} <$ 300 km s^{-1}, 180 km s^{-1} $< \sigma_{\rm spec} <$ 300 km s^{-1}, $\delta\sigma_{\rm spec}/\sigma_{\rm spec} < 0.15$ and $10.8\ h_{70}^{-1} M_{\odot} < \log(M_*) < 11.5\ h_{70}^{-1} M_{\odot}$. However, if we simultaneously select on stellar mass and model velocity dispersion, we implicitly also select on effective radius and Sérsic index. This is demon-

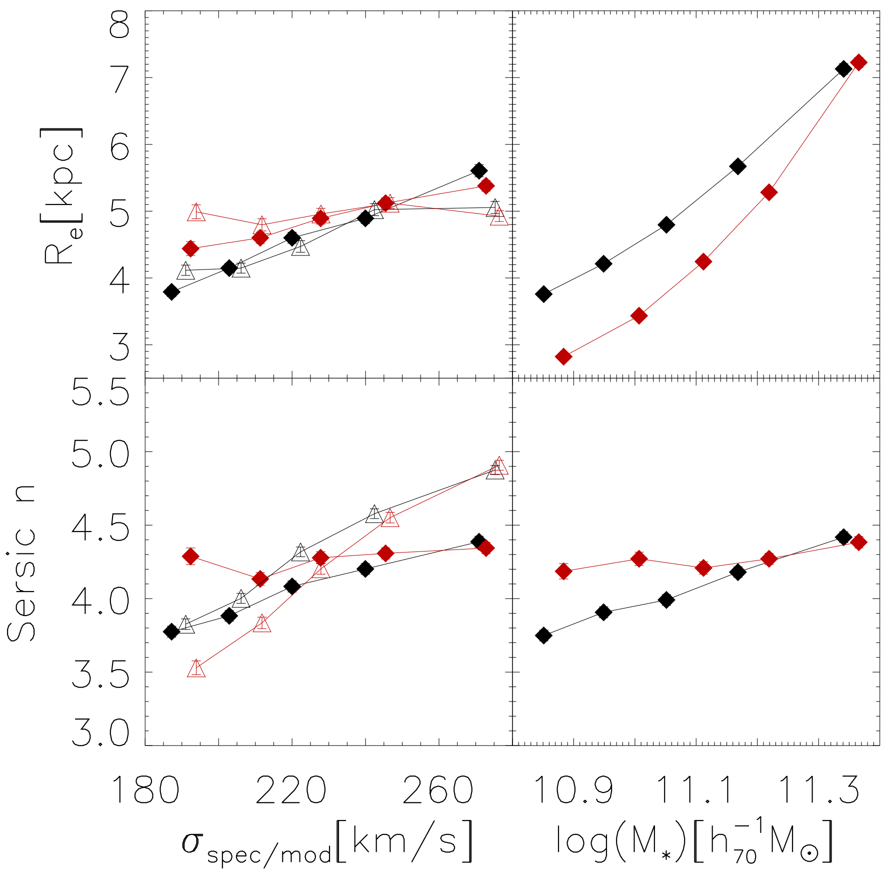

Figure 4.6: Mean effective radius and Sérsic index as a function of spectroscopic velocity dispersion (*left, black filled diamonds*), model velocity dispersion (*left, black open triangles*) and stellar mass (*right, black diamonds*). In red, we show the averages for the lens samples that simultaneously satisfy 180 km s^{-1} < σ_{mod} < 300 km s^{-1}, 180 km s^{-1} < σ_{spec} < 300 km s^{-1}, $\delta\sigma_{spec}/\sigma_{spec} < 0.15$ and $10.8\, h_{70}^{-1} M_\odot < \log(M_*) < 11.5\, h_{70}^{-1} M_\odot$. By simultaneously applying all selection criteria the average sizes and Sérsic indices of the samples change, which shows that we implicitly exclude galaxies from a certain area of structural parameter space.

strated in Figure 4.6 and Figure 4.7, where we show the mean effective radius and Sérsic index for the lens samples. When we select lenses that pass all selection criteria, we exclude lenses with large effective radii and small Sérsic indices at low stellar mass, lenses with small effective radii and small Sérsic indices at low spectroscopic velocity dispersions, and lenses with small effective radii and large Sérsic indices at low model velocity dispersions. If the lensing signal of a galaxy also depends on its structural parameters, the lensing measurements of this fourth sample could be biased, making the results harder to interpret.

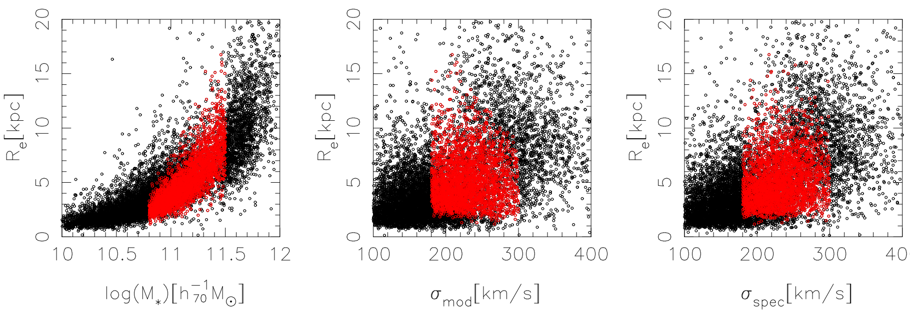

Figure 4.7: The effective radius as a function of stellar mass (*left*), model velocity dispersion (*middle*) and spectroscopic velocity dispersion (*middle*). The black dots show all de Vaucouleur galaxies with $z < 0.2$, the red dots are the lenses that satisfy 180 km s^{-1} $< \sigma_{\rm mod} <$ 300 km s^{-1}, 180 km s^{-1} $< \sigma_{\rm spec} <$ 300 km s^{-1}, $\delta\sigma_{\rm spec}/\sigma_{\rm spec} < 0.15$ and $10.8\ h_{70}^{-1} M_\odot < \log(M_*) < 11.5\ h_{70}^{-1} M_\odot$. By using all selection criteria simultaneously, we exclude large galaxies at low stellar masses and high model velocity dispersions, and small galaxies in the velocity dispersion samples. These selection biases could bias the lensing analysis if the lensing signal of a galaxy also depends on the effective radius.

4.4 Conclusion

In this work, we study which property of galaxies is most tightly correlated to the weak gravitational lensing signal on small scales. The properties we compare are the stellar mass, the spectroscopic velocity dispersion and the model velocity dispersion. We find that the lensing signal of galaxies is equally well traced by the stellar mass and the spectroscopic velocity dispersion. There is a weak indication for a residual dependence on stellar mass after removing the trend with spectroscopic velocity dispersion, and vice versa. This suggests that both tracers contain independent information on the projected distribution of dark matter around galaxies. Unfortunately, the signal-to-noise of our lensing measurements is not sufficient to make a definite statement.

The model velocity dispersion traces the lensing signal significantly worse, which is surprising as the spectroscopic velocity dispersion and model velocity dispersion correlate well for our lenses. At high velocity dispersions, however, the lenses in the $\sigma_{\rm mod}$-sample have smaller effective radii and larger Sérsic indices than those in the $\sigma_{\rm spec}$-sample. This suggests that these structural parameters contain additional information on the projected distribution of dark matter around galaxies. To test this, we measure how the lensing signal depends on the size and Sérsic index of the lenses. We do not find conclusive evidence for a residual dependence on these structural parameters, which could be due to insufficient signal-to-noise caused by the relatively small lens sample of this study.

The lensing signal on small projected separations from the lenses mainly depends on the halo mass. Our results therefore suggest that the stellar mass and spectroscopic velocity dispersion trace the halo mass equally well, but the model velocity dispersion does worse. However, at larger separations, neighbouring structures contribute to the lensing signal as well, and we cannot exclude the possibility that differences between the clustering properties of the lens samples also has some effect. To account for the clustering properties of the galaxies, and remove their contribution from the lensing signal, we could model the lensing signal using the halo model formalism (Seljak 2000; Cooray & Sheth 2002). An additional advantage of this approach would be that it enables a simultaneous study of the halo mass and the clustering properties of galaxies. We postpone this analysis to a future work.

Ideally, one should also remove the potential lensing signal dependence on the structural parameters of galaxies, i.e. split the lens sample both in velocity dispersion and structural parameters, and study the residual dependence on stellar mass. With the current data, we do not have sufficient signal-to-noise to perform such an analysis. Ultimately, one could simultaneously fit all these parameters, i.e. $M_h = f(\sigma, M_*, r_e, n, ...)$, which could also contain products of the parameters such as σM_*, and determine the covariance matrix between the coefficients. The relative magnitude of the coefficients would give new insights into which observables are important, and hence would provide valuable insights into galaxy formation processes.

Acknowledgements

We would like to thank Pieter van Dokkum and David Wake for useful discussions. HH and EvU acknowledge support from a Marie Curie International Reintegration Grant. HH is also supported by a VIDI grant from the Nederlandse Organisatie voor Wetenschappelijk Onderzoek (NWO). MDG thanks the Research Corporation for support via a Cottrell Scholars Award. The RCS2 project is supported in part by grants to HKCY from the Canada Research Chairs program and the Natural Science and Engineering Research Council of Canada.

This work is based on observations obtained with MegaPrime/MegaCam, a joint project of CFHT and CEA/DAPNIA, at the Canada-France-Hawaii Telescope (CFHT) which is operated by the National Research Council (NRC) of Canada, the Institute National des Sciences de l'Univers of the Centre National de la Recherche Scientifique of France, and the University of Hawaii. We used the facilities of the Canadian Astronomy Data Centre operated by the NRC with the support of the Canadian Space Agency.

Bibliography

Abazajian, K. N., Adelman-McCarthy, J. K., Agüeros, M. A., et al. 2009, ApJS, 182, 543

Adelman-McCarthy, J. K., Agüeros, M. A., Allam, S. S., et al. 2008, ApJS, 175, 297

Bertin, E. & Arnouts, S. 1996, A&AS, 117, 393

Bertin, G., Ciotti, L., & Del Principe, M. 2002, A&A, 386, 149

Bezanson, R., van Dokkum, P. G., Franx, M., et al. 2011, ApJ, 737, L31

Blanton, M. R., Schlegel, D. J., Strauss, M. A., et al. 2005, AJ, 129, 2562

Cappellari, M., Bacon, R., Bureau, M., et al. 2006, MNRAS, 366, 1126

Cooray, A. & Sheth, R. 2002, Phys. Rep., 372, 1

Eisenstein, D. J., Annis, J., Gunn, J. E., et al. 2001, AJ, 122, 2267

Erben, T., Hildebrandt, H., Lerchster, M., et al. 2009, A&A, 493, 1197
Erben, T., Schirmer, M., Dietrich, J. P., et al. 2005, Astronomische Nachrichten, 326, 432
Faber, S. M. & Jackson, R. E. 1976, ApJ, 204, 668
Gilbank, D. G., Gladders, M. D., Yee, H. K. C., & Hsieh, B. C. 2011, AJ, 141, 94
Graves, G. J., Faber, S. M., & Schiavon, R. P. 2009, ApJ, 693, 486
Guo, Q., White, S., Li, C., & Boylan-Kolchin, M. 2010, MNRAS, 404, 1111
Hoekstra, H., Franx, M., & Kuijken, K. 2000, ApJ, 532, 88
Hoekstra, H., Franx, M., Kuijken, K., & Squires, G. 1998, ApJ, 504, 636
Ilbert, O., Arnouts, S., McCracken, H. J., et al. 2006, A&A, 457, 841
Kaiser, N., Squires, G., & Broadhurst, T. 1995, ApJ, 449, 460
Komatsu, E., Smith, K. M., Dunkley, J., et al. 2011, ApJS, 192, 18
Koopmans, L. V. E., Bolton, A., Treu, T., et al. 2009, ApJ, 703, L51
Leauthaud, A., Tinker, J., Bundy, K., et al. 2012, ApJ, 744, 159
Luppino, G. A. & Kaiser, N. 1997, ApJ, 475, 20
Mandelbaum, R., Seljak, U., Kauffmann, G., Hirata, C. M., & Brinkmann, J. 2006, MNRAS, 368, 715
More, S., van den Bosch, F. C., Cacciato, M., et al. 2011, MNRAS, 410, 210
Moster, B. P., Somerville, R. S., Maulbetsch, C., et al. 2010, ApJ, 710, 903
Padmanabhan, N., Schlegel, D. J., Finkbeiner, D. P., et al. 2008, ApJ, 674, 1217
Seljak, U. 2000, MNRAS, 318, 203
Smith, R. J., Lucey, J. R., & Hudson, M. J. 2009, MNRAS, 400, 1690
Strauss, M. A., Weinberg, D. H., Lupton, R. H., et al. 2002, AJ, 124, 1810
Taylor, E. N., Franx, M., Brinchmann, J., van der Wel, A., & van Dokkum, P. G. 2010, ApJ, 722, 1
Treu, T. & Koopmans, L. V. E. 2004, ApJ, 611, 739
van Uitert, E., Hoekstra, H., Velander, M., et al. 2011, A&A, 534, A14
Wake, D. A., Whitaker, K. E., Labbé, I., et al. 2011, ApJ, 728, 46
York, D. G., Adelman, J., Anderson, Jr., J. E., et al. 2000, AJ, 120, 1579